Lanthanide-doped $NaYF_4$ near-infrared-II nanothermometers for deep tissue temperature sensing

Yuan, Xiangyang; Cui, Endian; Liu, Kai; Jiang, Ying; Yang, Xiaoyan; Tang, Jianfeng; Yang, Lu; Liao, Xiaoling; Zhao, Yanan; More Authors

DOI
10.1016/j.ceramint.2022.08.110

Publication date
2022

Document Version
Final published version

Published in
Ceramics International

Ceramics International 48 (2022) 35141–35149

Contents lists available at ScienceDirect

Ceramics International

journal homepage: www.elsevier.com/locate/ceramint

Lanthanide-doped $NaYF_4$ near-infrared-II nanothermometers for deep tissue temperature sensing

Xiangyang Yuan [a], Endian Cui [a], Kai Liu [b], Ying Jiang [a], Xiaoyan Yang [a], Jianfeng Tang [a], Lu Yang [a], Xiaoling Liao [a], Yanan Zhao [c], Wei Sun [d], Yingshuai Liu [a,**], Jing Liu [a,*]

[a] Key Laboratory of Luminescence Analysis and Molecular Sensing, Ministry of Education, School of Materials and Energy, Southwest University, Chongqing, 400715, PR China
[b] Materials for Energy Conversion and Storage, Department of Chemical Engineering, Delft University of Technology, Delft, 2629 HZ, the Netherlands
[c] Analytical and Testing Center, Southwest University, Chongqing, 400715, PR China
[d] Key Laboratory of Laser Technology and Optoelectronic Functional Materials of Hainan Province, College of Chemistry and Chemical Engineering, Hainan Normal University, Haikou 571158, PR China

ARTICLE INFO

Keywords:
Lanthanide-doped
Nanothermometers
Second near-infrared region
Energy transfer
Biocompatibility

ABSTRACT

In this work, different lanthanides (Tm^{3+}, Er^{3+}; Yb^{3+}, Ho^{3+}, Nd^{3+}) were doped into $NaYF_4$ via a high-temperature coprecipitation method, and followed by SiO_2 coating to improve the water dispersibility, resulting in $NaYF_4$:Tm^{3+}, Er^{3+}@$NaYF_4$@SiO_2 and $NaYF_4$:Yb^{3+}, Ho^{3+}@$NaYF_4$:Nd^{3+}@SiO_2 nanoparticles (NPs). The two NPs both exhibited the temperature-dependent second near-infrared (NIR-II) downshifting luminescence over the physiological range. The luminescence ratio of Tm^{3+} emission at 1460 nm to Er^{3+} emission at 1525 nm (Tm^{3+}:$^3H_4 \rightarrow {}^3F_4$; Er^{3+}:$^4I_{13/2} \rightarrow {}^4I_{13/2}$) varies with temperature increase, as well as Yb^{3+} emission at 980 nm and Ho^{3+} emission at 1150 nm (Yb^{3+}:$^2F_{5/2} \rightarrow {}^2F_{7/2}$; Ho^{3+}:$^5I_6 \rightarrow {}^5I_8$). The highest relative sensitivity of $NaYF_4$:Tm^{3+}, Er^{3+}@$NaYF_4$@SiO_2 and $NaYF_4$:Yb^{3+}, Ho^{3+}@$NaYF_4$:Nd^{3+}@SiO_2 aqueous suspension is 0.36% K^{-1} (at 298 K) and 0.76% K^{-1} (at 343 K), respectively. The biological tests prove the good biocompatibility and low toxicity of the water-soluble NPs. *In vitro* tissue penetration experiments verify a much better penetration ability of the synthesized $NaYF_4$:Tm^{3+}, Er^{3+}@$NaYF_4$@SiO_2 compared with $NaYF_4$:Yb^{3+}, Ho^{3+}@$NaYF_4$:Nd^{3+}@SiO_2 NPs. The excellent physiological luminescent thermometry with favor wave penetration depth provides a promising platform in deep tissue temperature measurement, which is very important in vivo biosensing.

1. Introduction

Accurate temperature measurement plays a very important role in the development of technology. The temperature measuring devices can be divided into contact thermometers and contactless thermometers [1, 2]. The traditional contact thermometers have certain limitations in their usage, especially nowadays the test objects have changed from macro-scale to micro-scale, such as electronic components, microbial cells, etc. While contactless temperature measurement device can accurately and quickly detect the internal temperature of target object without system calibration, and the measurement results are not affected by medium changes [3–8]. Luminescent nanothermometer, one of contactless temperature measurement devices, is based on the temperature-dependent luminescence changes, such as emission intensity, luminescent lifetime, spectral linewidth, polarization direction, or the intensity ratio between two emission peaks. Lanthanide-doped luminescent materials have demonstrated their great potential in the field of temperature sensing due to the advantages of good photostability and chemical stability, narrow-band emission, tunable emission wavelength, long luminescent lifetime [9–13].

Compared to ultraviolet (UV) and visible light, the near-infrared (NIR) light has lower scattering and autofluorescence, high penetration depth in biological tissues [14–17]. The NIR window can be divided into the first NIR region (NIR-I, 650–1000 nm) and the second NIR region (NIR-II, 1000–1500 nm) [18]. The Ln luminescence emits the emission from UV to NIR, and the NIR-II light can be obtained by the choice of Ln^{3+}. Therefore, Ln^{3+}-doped luminescent NPs were developed for temperature sensors. Marcin Runowski et al. obtained water

* Corresponding author.
** Corresponding author.
E-mail addresses: ysliu@swu.edu.cn (Y. Liu), jingliu77@swu.edu.cn (J. Liu).

https://doi.org/10.1016/j.ceramint.2022.08.110
Received 18 June 2022; Received in revised form 19 July 2022; Accepted 9 August 2022
Available online 15 August 2022

dispersible β-$NaYF_4$:Yb^{3+}, Er^{3+}@SiO_2 nanorods for a bright dual-center physiological thermometer (λ_{ex} = 975 nm), based on the intensity ratio of Yb^{3+}/Er^{3+} at 1010 nm/810 nm ($^2F_{5/2} \rightarrow {}^2F_{7/2}/{}^4I_{9/2} \rightarrow {}^4I_{15/2}$) or Yb^{3+}/Er^{3+} at 1010 nm/660 nm ($^2F_{5/2} \rightarrow {}^2F_{7/2}/{}^2F_{9/2} \rightarrow {}^4I_{15/2}$), obtaining the thermal sensitive (S_r) up to 1.64% K^{-1} or 0.96% K^{-1}, respectively [19]. Li et al. successfully synthesized novel flower-like α-NaYb(Mn)F_4:Tm^{3+}@$NaYF_4$ NPs. The synthesized NPs exhibits strong upconversion luminescence and temperature dependence performance ranging from 123 K to 423 K, with S_r of 0.24% K^{-1} at 123 K. The intensity ratios of Tm^{3+} ($^1G_4 \rightarrow {}^3H_5$ and $^4F_{9/2} \rightarrow {}^4I_{15/2}$) NIR-I emission bands at 776 nm and 803 nm change regularly with the increased temperature [20]. However, those reported luminescent nanothermometers have not yet been able to achieve precise and real-time physiological temperature sensors in deep tissues. Therefore, it is imperative to design a physiological luminescent nanothermometer with a deep penetration depth and good biocompatibility.

In this work, we first synthesized two NIR-II downshifted emitting NPs ($NaYF_4$:Tm^{3+}, Er^{3+}@$NaYF_4$@SiO_2 and $NaYF_4$:Yb^{3+}, Ho^{3+}@$NaYF_4$:Nd^{3+}@SiO_2), and their morphologies and structures were characterized. The temperature dependence of optical properties and the performance of luminescence thermometers was also evaluated. In order to explore the optical thermometry application in the deep tissue, in vitro hemolysis, cytotoxicity, mouse blood biochemistry, histology analysis and in vitro tissue penetration experiments were conducted.

2. Experimental section

2.1. Materials

$Y(CH_3CO_2)_3{\cdot}4H_2O$ (99.9%), $Yb(CH_3CO_2)_3{\cdot}4H_2O$ (99.9%), $Tm(CH_3CO_2)_3{\cdot}4H_2O$ (99.9%), $Ho(CH_3CO_2)_3{\cdot}4H_2O$ (99.9%), $Er(CH_3CO_2)_3{\cdot}4H_2O$ (99.9%), $Nd(CH_3CO_2)_3{\cdot}4H_2O$ (99.9%), ammonium fluoride (NH_4F, 99.99%), cyclohexane (99.5%), 1-octadecene (ODE, 90%), oleic acid (OA, 90%), sodium oleate (96%), sodium hydroxide (NaOH, 96%), methanol (99.5%), tetraethyl orthosilicate (99.99%), Igepal CO-520 and ammonia solution (25%) were purchase from Sigma-Aldrich. All chemicals were used without any further purification.

2.2. Synthesis of α-$NaYF_4$:Ln^{3+} NPs

For the synthesis of α-$NaYF_4$:2%Tm^{3+}, 5%Er^{3+}, 0.744 mmol $Y(CH_3CO_2)_3{\cdot}4H_2O$, 0.016 mmol $Tm(CH_3CO_2)_3{\cdot}4H_2O$ and 0.04 mmol $Er(CH_3CO_2)_3{\cdot}4H_2O$ were mixed with 5.0 mL OA and 5.0 mL ODE in a three-neck flask. The solution was heated to 100 °C under vacuum, and maintained 30 min. Afterwards sodium oleate was added, and the solution was then degassed under vacuum for 15 min to form a clear solution. Thereafter, 5.0 mL methanol solution with 3.2 mmol ammonium fluoride was added to the mixture under N_2 flow. Then, the mixed solution was degassed under vacuum for 30 min, and then heated to 200 °C for 1 h under N_2 flow. After cooling down to room temperature, the resulting NCs were precipitated by the addition of ethanol, and washed twice with ethanol.

For the synthesis of α-$NaYF_4$:30%Yb^{3+}, 5%Ho^{3+}, 0.52 mmol $Y(CH_3CO_2)_3{\cdot}4H_2O$, 0.24 mmol $Yb(CH_3CO_2)_3{\cdot}4H_2O$ and 0.04 mmol $Ho(CH_3CO_2)_3{\cdot}4H_2O$ were mixed with 5.0 mL OA and 5.0 mL ODE in a three-neck flask. The rest of the steps are the same as mentioned above.

2.3. Synthesis of β-$NaYF_4$:Ln^{3+} NPs

The α-$NaYF_4$:Ln^{3+} NPs were dissolved in the mixture of 5.0 mL of ODE and 5.0 mL of OA, followed by outgassing at 100 °C for 30 min under vacuum, then the mixture was heated to 300 °C under N_2 flow for 90 min with a heating rate of 10 °C min^{-1}. After the solution was cooled down to room temperature, the colloidal solution was washed by ethanol for three times.

2.4. Synthesis of core-shell NPs

For the synthesis of β-$NaYF_4$:2%Tm^{3+}, 5%Er^{3+}@β-$NaYF_4$, 0.8 mmol as-synthesized α-$NaYF_4$ and 0.8 mmol β-$NaYF_4$:2%Tm^{3+}, 5%Er^{3+} were dissolved in the mixture of 5.0 mL of ODE and 5.0 mL of OA, followed by outgassing at 100 °C for 30 min under vacuum. Then, the mixture was heated to 300 °C under N_2 flow for 90 min with a heating rate of 10 °C min^{-1}. After cooling down, the colloidal solution was washed by ethanol for three times.

For the synthesis of β-$NaYF_4$:30%Yb^{3+}, 5%Ho^{3+}@β-$NaYF_4$:30% Nd^{3+}, the synthesized steps are the same as the aforementioned β-$NaYF_4$:2%Tm^{3+}, 5%Er^{3+}@β-$NaYF_4$, except 0.8 mmol α-$NaYF_4$: 30% Nd^{3+} and 0.8 mmol β-$NaYF_4$:30%Yb^{3+}, 5%Ho^{3+} were dissolved in the mixture of 5.0 mL of ODE and 5.0 mL of OA, instead of 0.8 mmol α-$NaYF_4$ and 0.8 mmol β-$NaYF_4$:2%Tm^{3+}, 5%Er^{3+}.

2.5. Synthesis of SiO_2 coated NPs

0.1 mL CO-520, 6 mL cyclohexane and 4 mL of 0.01 mol/L $NaYF_4$ cyclohexane solution were mixed and stirred for 10 min. Then 0.4 mL CO-520 and 0.08 mL of 30% (by mass) ammonia water solution was added, sealed and ultrasonically shaken for 20 min until a transparent emulsion was formed. 0.04 mL ethyl orthosilicate was then added to the solution and stirred at 600 rpm for two days. The resulting NPs were precipitated by the addition of acetone, washed twice with ethanol/water (1:1 V/V) and dispersed in water.

2.6. Characterization

X-ray diffraction (XRD) measurements were performed on a Shimadzu XRD-7000 diffractometer with Cu K_α (λ = 1.54 Å) radiation in the 2θ range from 10 to 90°. The photoluminescence spectra were recorded on an Edinburgh Fluorescence Spectrometer FLS1000 with the excitation source of external 808 nm and 1208 nm continuous-wave diode lasers (Changchun New Industries Optoelectronics). Transmission Electron Microscope (TEM) studies were performed on a JEOL JEM 2100F filed emission electron microscope equipped with the energy dispersive X-ray spectrum (EDS). Fourier transform infrared (FT-IR) spectroscopy studies was carried out using a PerkinElmer Spectrum Two spectrometer. The NIR-II window fluorescence images were collected by a digital visible-short-wave infrared InGaAs camera (Raptor Launches Ninox1280) along with long-pass emission filters (1300 nm longpass, 935 nm longpass).

2.7. Cytotoxicity assay and in vitro hemolysis assay

The cytotoxicity of $NaYF_4$:Yb^{3+}, Ho^{3+}@$NaYF_4$:Nd^{3+}@SiO_2 and $NaYF_4$:Tm^{3+}, Er^{3+}@$NaYF_4$@SiO_2 was assessed by cell counting kit-8 (CCK-8) assay kit, and L929 mouse fibroblasts were used for cytotoxicity experiments. The cells were seeded into 96-well plates, and complete medium was added. The number of cells in each well was 5000. After 24 h incubation, 0, 50, 100, 150, and 200 μg/mL of $NaYF_4$:Yb^{3+}, Ho^{3+}@$NaYF_4$:Nd^{3+}@SiO_2 and $NaYF_4$:Tm^{3+}, Er^{3+}@$NaYF_4$@SiO_2 solution were added to each well to replace the original culture medium. The medium was removed from the well plate after 24 h of incubation, 100 μL CCK-8 solution was added to each well, and incubated for 1.5 h. Then the absorption at 450 nm was tested with a microplate reader.

The hemolysis assay experiments were carried out to evaluate in vitro biocompatibility of synthesized SiO_2 coated NPs. 2 mL of whole blood in anticoagulant sodium citrate was obtained from BALB/c mice. The whole blood was diluted by adding 2 mL of PBS buffer, then centrifuged at 1000 rpm for 10 min, the supernatant was removed to obtain red blood cells, and the obtained red blood cells were re-dispersed in 2 mL of PBS buffer. 0.1 mL of the dispersed red blood cell suspension was mixed with 0.9 mL of PBS as a negative control, 0.9 mL of distilled water as a positive control. 0.9 mL of $NaYF_4$:Yb^{3+},

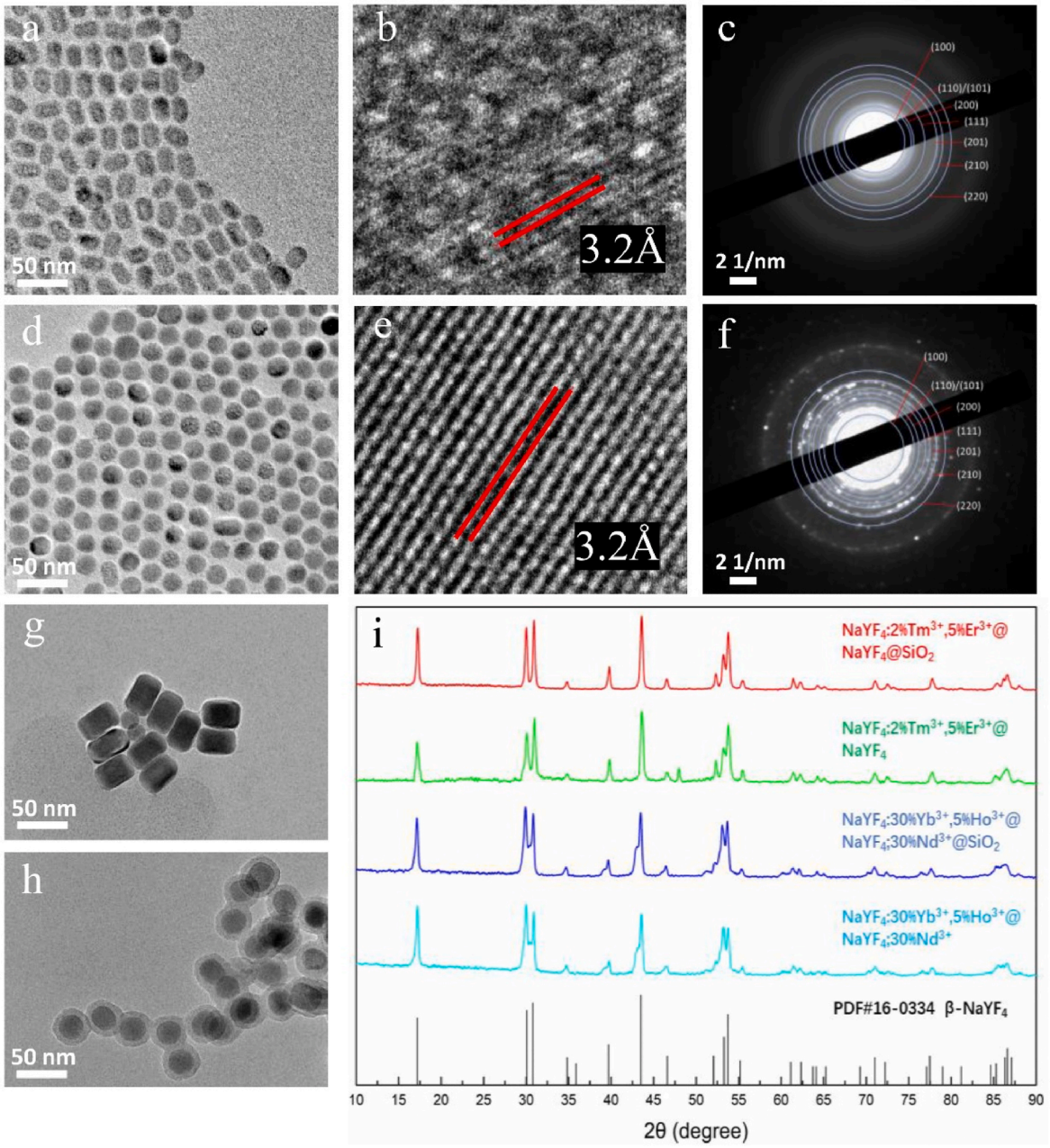

Fig. 1. (a, d, g, h) TEM images of $NaYF_4$:Tm^{3+}, Er^{3+}@$NaYF_4$, $NaYF_4$:Yb^{3+}, Ho^{3+}@$NaYF_4$:Nd^{3+}, $NaYF_4$:Tm^{3+}, Er^{3+}@$NaYF_4$@SiO_2 and $NaYF_4$:Yb^{3+}, Ho^{3+}@$NaYF_4$:Nd^{3+}@SiO_2 NPs, (b, e) HRTEM images of $NaYF_4$:Yb^{3+}, Ho^{3+}@$NaYF_4$: Nd^{3+} and $NaYF_4$:Tm^{3+}, Er^{3+}@$NaYF_4$ NPs. (c, f) The selected area electron diffraction (SAED) pattern of $NaYF_4$:Tm^{3+}, Er^{3+}@$NaYF_4$ NPs and $NaYF_4$:Yb^{3+}, Ho^{3+}@$NaYF_4$: Nd^{3+} NPs. (i) XRD patterns of $NaYF_4$:Tm^{3+}, Er^{3+}@$NaYF_4$, $NaYF_4$:Yb^{3+}, Ho^{3+}@$NaYF_4$:Nd^{3+}, $NaYF_4$:Tm^{3+}, Er^{3+}@$NaYF_4$@SiO_2 and $NaYF_4$:Yb^{3+}, Ho^{3+}@$NaYF_4$:Nd^{3+}@SiO_2 NPs.

Ho^{3+}@$NaYF_4$:Nd^{3+}@SiO_2 NPs were dissolved in PBS at concentrations of 0, 1.25, 2.5, and 5 mg/mL as experimental groups, and incubated at 37 °C for 6 h. The solution was centrifuged at 10,000 rpm for 5 min, and the absorbance of the supernatant was measured at 540 nm. Hemolysis rate = (sample absorbance − absorbance of negative control)/(absorbance of positive control − absorbance of negative control) × 100%.

2.8. Blood biochemistry and histology analysis

BALB/c mice were used for the blood routine test. Nine mice were divided into three groups, 1 mg/mL $NaYF_4$:Tm^{3+}, Er^{3+}@$NaYF_4$@SiO_2 and $NaYF_4$:Yb^{3+}, Ho^{3+}@$NaYF_4$:Nd^{3+}@SiO_2 in PBS buffer solution were prepared. The mice were injected with 200 μL of two solution via the tail vein, respectively. The injection of the same amount of PBS buffer solution was served as a control group, and blood samples were collected from the fundus artery of the mice three days later. The main organs, including heart, liver, spleen, lung, kidney, were fixed with formaldehyde solution, and stained with hematoxylin-eosin (H&E). The H&E staining histological images were collected by an inverted fluorescence microscope (Olympus IX71).

2.9. In vitro penetration depth test

5 mg/mL of $NaYF_4$:Tm^{3+}, Er^{3+}@$NaYF_4$@SiO_2 and $NaYF_4$:Yb^{3+}, Ho^{3+}@$NaYF_4$:Nd^{3+}@SiO_2 aqueous solutions were prepared. The solutions were then added to a 96-well plate, different pieces of 1, 3, 6, 9 mm thick pork muscle tissue was placed above the plates, and excited with 1208 nm and 808 nm lasers with the same power density (15W/cm^2),

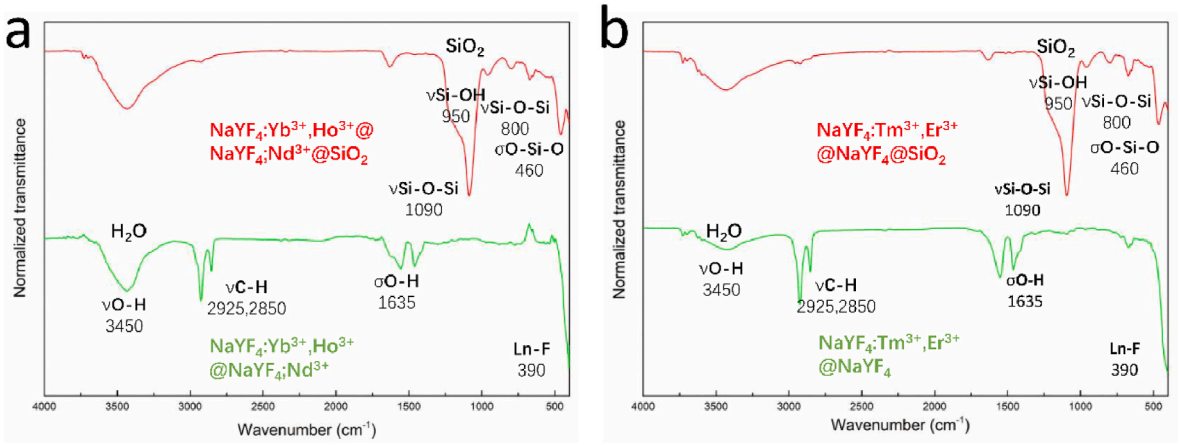

Fig. 2. (a) FT-IR spectra of $NaYF_4$:Yb^{3+}, Ho^{3+}@$NaYF_4$:Nd^{3+}@SiO_2 and $NaYF_4$:Yb^{3+}, Ho^{3+}@$NaYF_4$:Nd^{3+} NPs. (b) FT-IR spectra of $NaYF_4$:Tm^{3+}, Er^{3+}@$NaYF_4$@ SiO_2 and $NaYF_4$:Tm^{3+}, Er^{3+}@$NaYF_4$ NPs. Absorption spectra of $NaYF_4$:Tm^{3+}, Er^{3+}@$NaYF_4$@ SiO_2 (c) and $NaYF_4$:Yb^{3+}, Ho^{3+}@$NaYF_4$:Nd^{3+}@SiO_2 (d).

respectively. And the NIR-II fluorescence images were obtained by a digital InGaAs array detector (Raptor Ninox1280) with long-pass emission filters (1300 nm, 935 nm).

3. Results and discussion

3.1. Structure and morphology characterization

The synthesized oleic acid capped $NaYF_4$:Ln^{3+} NPs via a high-temperature coprecipitation method [21] have poor water solubility and biocompatibility. To improve the water solubility of $NaYF_4$ NPs,

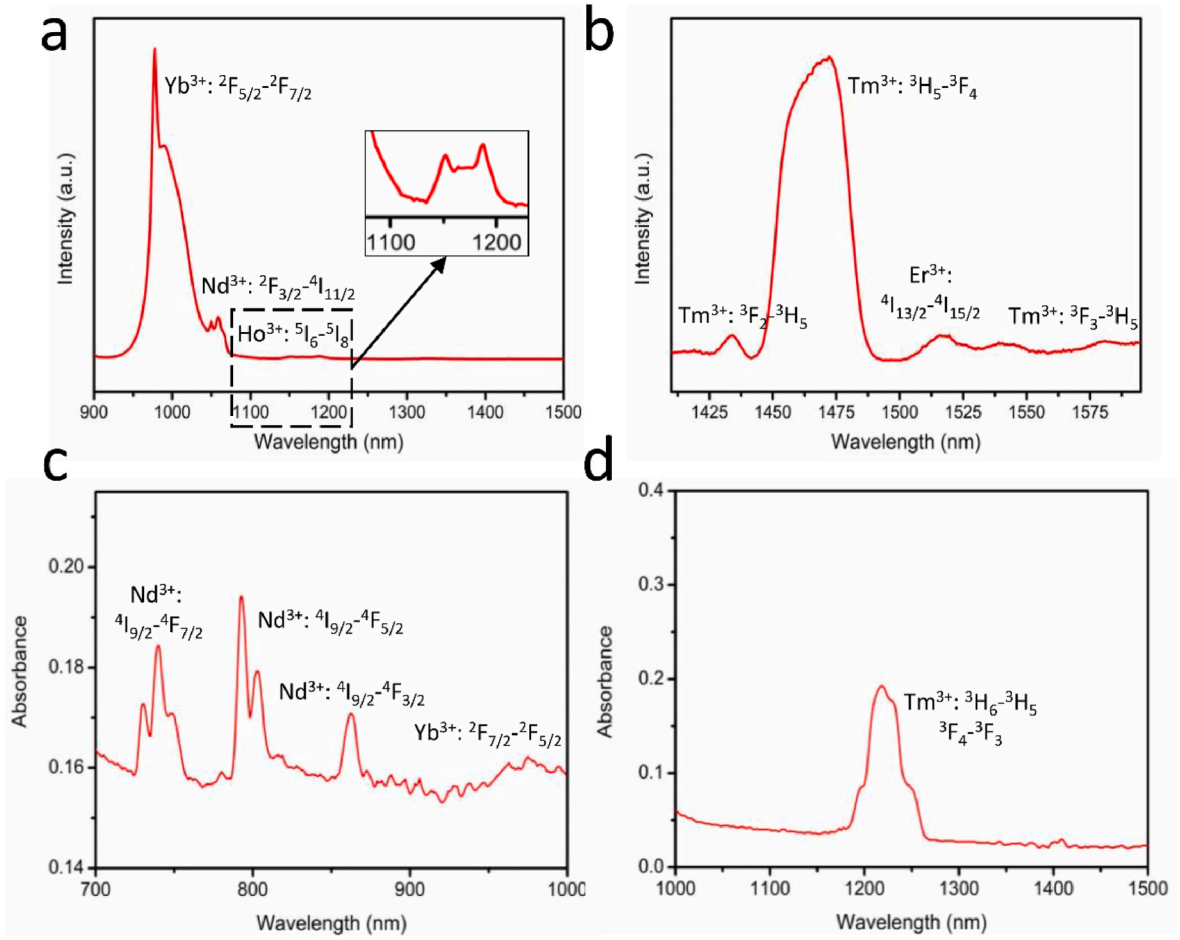

Fig. 3. (a) Room temperature luminescence emission spectrum of $NaYF_4$:Yb^{3+}, Ho^{3+} @$NaYF_4$:Nd^{3+}@SiO_2 aqueous suspension under excitation at 808 nm. (b) Room temperature luminescence emission spectrum of $NaYF_4$:Tm^{3+}, Er^{3+}@$NaYF_4$@SiO_2 aqueous suspension under excitation at 1208 nm. Absorption spectra of (c) $NaYF_4$:Yb^{3+}, Ho^{3+}@$NaYF_4$:Nd^{3+}@SiO_2 and (d)$NaYF_4$:Tm^{3+}, Er^{3+}@$NaYF_4$@SiO_2.

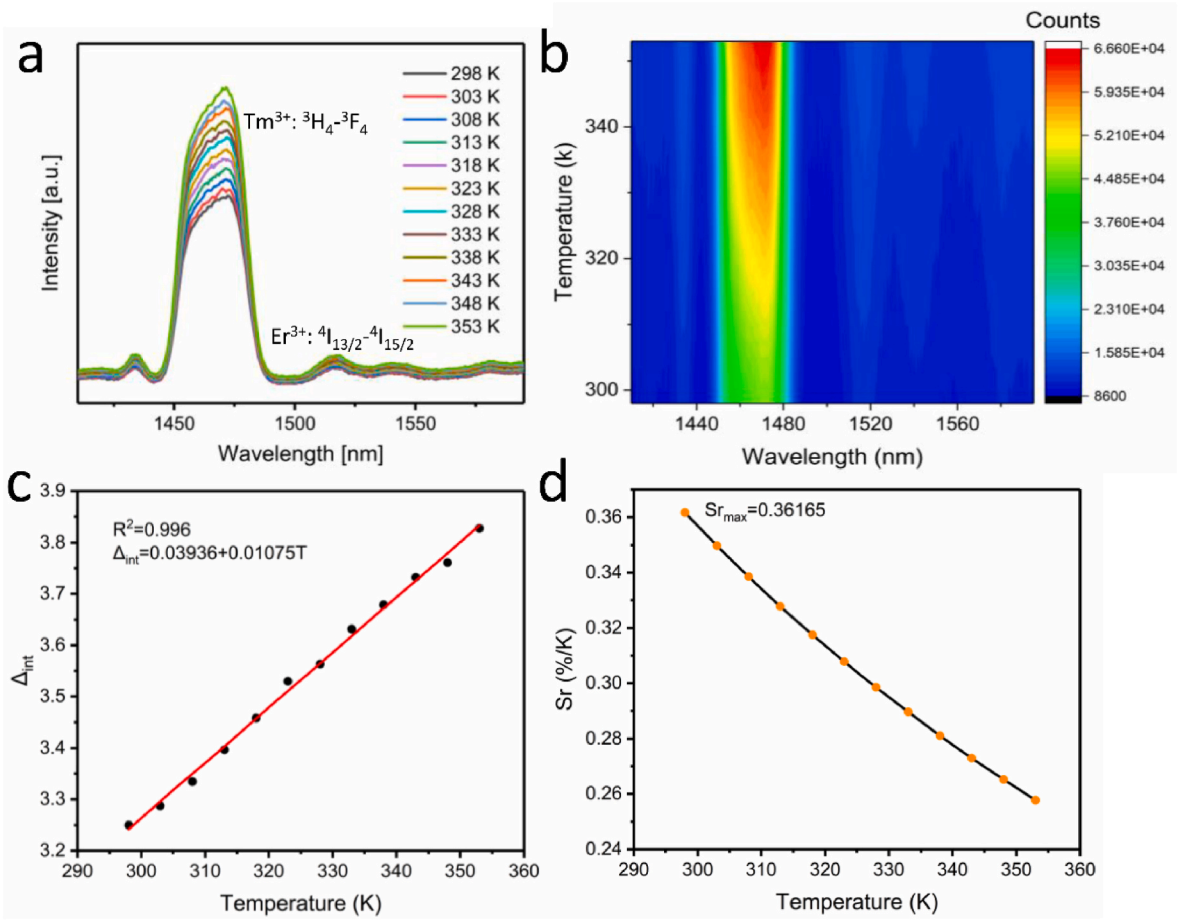

Fig. 4. (a, b) Temperature-dependent NIR emission spectra of $NaYF_4$:Tm^{3+}, Er^{3+}@$NaYF_4$@SiO_2 aqueous suspension under 1208 nm excitation. (c) Calibration curve for the relationship between Δ_{int} and temperature of $NaYF_4$:Tm^{3+}, Er^{3+}@$NaYF_4$@SiO_2 aqueous suspension. (d) S_r values at different temperatures for $NaYF_4$:Tm^{3+}, Er^{3+}@$NaYF_4$@SiO_2 aqueous suspension.

surface coating of silicon dioxide was chosen [22–24]. From Transmission Electron Microscope (TEM) images in Fig. 1a and b, we can see the shape of $NaYF_4$:Tm^{3+}, Er^{3+}@$NaYF_4$ NPs is roughly elliptical, and the particles size is of around 23.5 nm with a uniform size distribution. The corresponding high-resolution TEM (HRTEM) image of $NaYF_4$:Tm^{3+}, Er^{3+}@$NaYF_4$ NPs in Fig. 1b shows the high crystallinity of the NPs. The lattice fringes were measured to be 3.2 Å, which corresponds to the d-spacing for the (111) lattice planes of β-$NaYF_4$. TEM images represent the uniform spherical shape of $NaYF_4$:Yb^{3+}, Ho^{3+}@$NaYF_4$:Nd^{3+} (Fig. 1d and e) with the average size of 17.2 nm, and the corresponding HRTEM image in Fig. 1b also indicated the high crystallinity of the NPs. The d-spacing of lattice fringes were measured as 3.2 Å, corresponding to the (111) lattice planes of β-$NaYF_4$ [25]. $NaYF_4$: Tm^{3+}, Er^{3+}@$NaYF_4$ (Fig. 1a) is larger than that of $NaYF_4$: Yb^{3+}, Ho^{3+}@$NaYF_4$: Nd^{3+} (Fig. 1d). The difference in the morphology and size of the two NPs may be related to the doping concentration of Ln^{3+}.

SiO_2 coating could increase the size of NPs, but would not influence the shape. Fig. 1g shows the particle size of $NaYF_4$: Tm^{3+}, Er^{3+}@$NaYF_4$@SiO_2 NPs is around 32 nm, and the thickness of SiO_2 shell is about 9 nm. With regard to $NaYF_4$:Yb^{3+}, Ho^{3+}@$NaYF_4$:Nd^{3+}, the average size increases from 17.2 nm to 28 nm after SiO_2 coating, with a thickness of 10.8 nm. And element mappings measurements were presented to determine the element distribution. From the element mapping images (Fig. S2), we could see that all the elements of $NaYF_4$: Tm^{3+}, Er^{3+}@$NaYF_4$@SiO_2 and $NaYF_4$: Yb^{3+}, Ho^{3+}@$NaYF_4$: Nd^{3+}@SiO_2 NPs were evenly distributed.

X-ray diffraction (XRD) patterns in Fig. 1i shows that the diffraction peaks of $NaYF_4$:Tm^{3+}, Er^{3+}@$NaYF_4$ and $NaYF_4$:Yb^{3+}, Ho^{3+}@$NaYF_4$:Nd^{3+} both matches well with the standard hexagonal β-$NaYF_4$ (JCPDS No.16-0334) [26], and no other peaks were found. Similarly, the diffraction peaks of $NaYF_4$:Tm^{3+}, Er^{3+}@$NaYF_4$@SiO_2 and $NaYF_4$:Yb^{3+}, Ho^{3+}@$NaYF_4$:Nd^{3+}@SiO_2 were in good accordance with the standard hexagonal β-$NaYF_4$. SiO_2 coating would not influence the crystal structure of NPs, due to the amorphous SiO_2 has no diffraction peaks [27].

In order to identify the characteristic functional groups of the NPs, we measured the Fourier transform infrared (FT-IR) spectra of $NaYF_4$: Yb^{3+}, Ho^{3+}@$NaYF_4$:Nd^{3+}@SiO_2 and $NaYF_4$:Yb^{3+}, Ho^{3+}@$NaYF_4$:Nd^{3+} NPs (Fig. 2a), $NaYF_4$:Tm^{3+}, Er^{3+}@$NaYF_4$@SiO_2 and $NaYF_4$:Tm^{3+}, Er^{3+}@$NaYF_4$ NPs (Fig. 2b). The FT-IR spectra of $NaYF_4$:Yb^{3+}, Ho^{3+}@$NaYF_4$:Nd^{3+} NPs shows absorption peaks at 3450 cm^{-1} and 1635 cm^{-1}, which are caused by O–H stretching (ν) and deformation (σ) vibrations from water molecules attached to the surface of NPs. The absorption peaks at 2925 cm^{-1} and 2850 cm^{-1} are assigned to the $\nu_{C\text{-}H}$ vibration in the OA -capped $NaYF_4$. Additional absorption peaks were observed in the FT-IR spectra of $NaYF_4$:Yb^{3+}, Ho^{3+}@$NaYF_4$:Nd^{3+}@SiO_2 NPs, $\nu_{Si\text{-}O\text{-}Si}$ at 800 and 1090 cm^{-1}, $\nu_{Si\text{-}OH}$ at 950 cm^{-1}, and $\sigma_{Si\text{-}O}$ at 460 cm^{-1} [19], Fig. 2b shows the similar phenomenon as that observed in Fig. 2a. In conclusion, the above experimental results show that the SiO_2 coated NPs were successfully synthesized.

3.2. Luminescence properties

Next, we investigated the room temperature luminescence properties of $NaYF_4$:Tm^{3+}, Er^{3+}@$NaYF_4$@SiO_2 (Fig. 3a) and $NaYF_4$:Yb^{3+}, Ho^{3+}@$NaYF_4$:Nd^{3+}@SiO_2 aqueous solutions (Fig. 3b). The synthesized $NaYF_4$:Tm^{3+}, Er^{3+}@$NaYF_4$@SiO_2 NPs showed two main downshifted

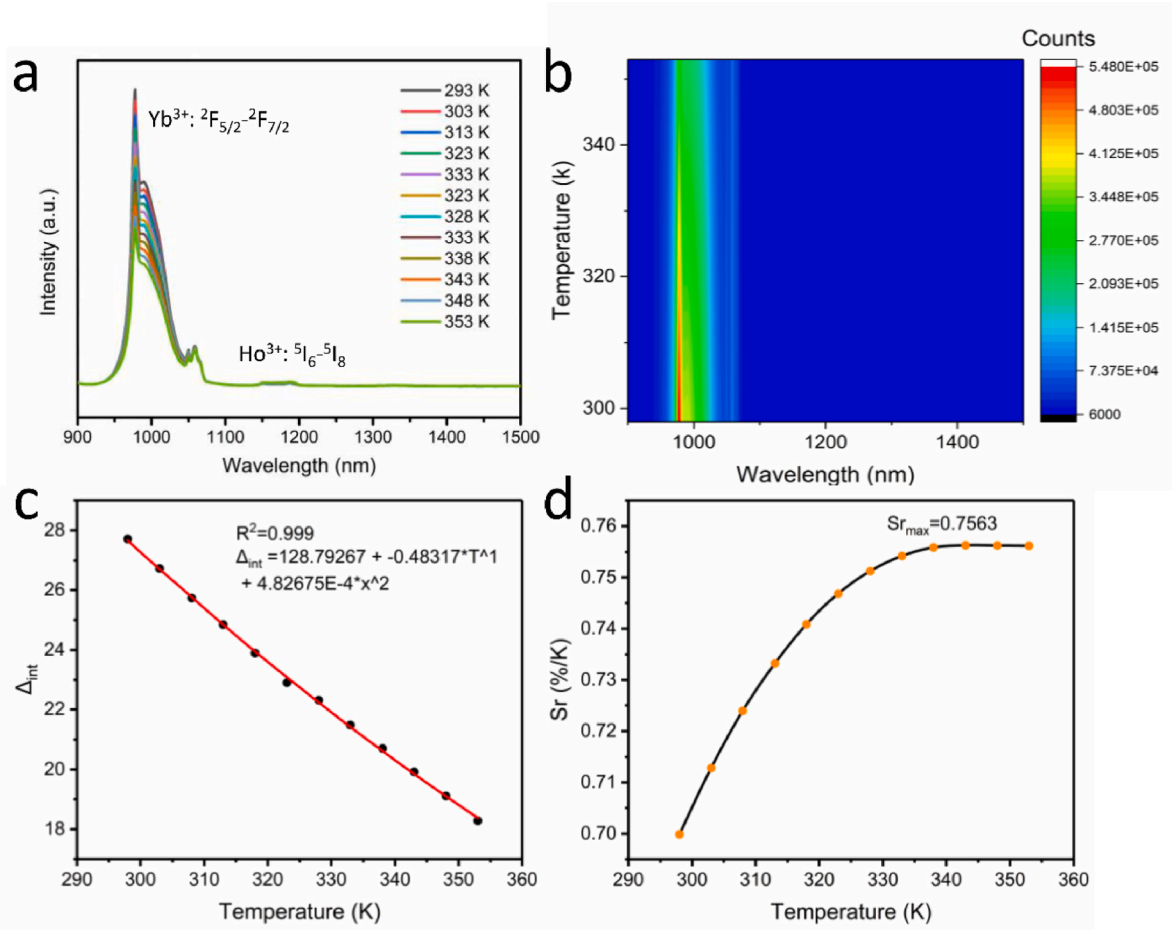

Fig. 5. (a, b) Temperature-dependent NIR emission spectra of $NaYF_4$:Yb^{3+}, Ho^{3+}@$NaYF_4$:Nd^{3+}@SiO_2 aqueous suspension under 808 nm excitation. (c) Calibration curve for the relationship between Δ_{int} and temperature of the $NaYF_4$:Yb^{3+}, Ho^{3+}@$NaYF_4$:Nd^{3+}@SiO_2 aqueous suspension. (d) S_r values at different temperatures for the $NaYF_4$:Yb^{3+}, Ho^{3+}@$NaYF_4$:Nd^{3+}@SiO_2 aqueous suspension.

emission peaks corresponding to $^3H_4 \rightarrow {}^3F_4$ transition (Tm^{3+}) at 1460 nm and $^4I_{13/2} \rightarrow {}^4I_{15/2}$ transition (Er^{3+}) at 1525 nm (Table S2) under 1208 nm excitation. $NaYF_4$:Yb^{3+}, Ho^{3+}@$NaYF_4$:Nd^{3+}@SiO_2 showed downshifting luminescence $^4F_{3/2} \rightarrow {}^4I_{11/2}$ emission of Nd^{3+} at 1060 nm, $^2F_{5/2} \rightarrow {}^2F_{7/2}$ emission of Yb^{3+}at 980 nm and $^5I_6 \rightarrow {}^5I_8$ emission of Ho^{3+} at 1150 nm (Table S1) under the laser excitation at 808 nm.

To further study the optical thermometric properties of NPs, the luminescence emission spectra of above two samples at different temperatures were characterized. Temperature-dependent NIR emission spectra of $NaYF_4$:Tm^{3+}, Er^{3+}@$NaYF_4$@SiO_2 aqueous suspension under 1208 nm excitation was presented in Fig. 4a, and its corresponding contour map is shown in Fig. 4b. When temperature increases from 298K to 353K, the integrated emission intensity of the $^3H_4 \rightarrow {}^3F_4$ transition of Tm^{3+} increases, while the integrated emission intensity of the $^4I_{13/2} \rightarrow {}^4I_{15/2}$ transition of Er^{3+} is nearly unchanged, suggesting that $NaYF_4$:Tm^{3+}, Er^{3+}@$NaYF_4$@SiO_2 has great potential in temperature sensing.

Temperature sensing performance of $NaYF_4$:Tm^{3+}, Er^{3+}@$NaYF_4$@SiO_2 were evaluated through calculating temperature parameter Δ_{int} (Fig. 4c) and relative thermal sensitivity S_r (Fig. 4d). Δ_{int} can be calculated by using the following formula:

$$\Delta_{int} = \frac{I_{Tm}}{I_{Er}} = \frac{\Delta_0}{1 + \alpha \exp(-\frac{\Delta E}{k_B T})} \quad 1$$

Where I_{Tm} and I_{Er} are the integrated emission intensity of Tm^{3+} at 1460 nm and Er^{3+} at 1525 nm, respectively; Δ_0 is thermometric parameter at T = 0 K; α is a constant depending on the ratio between nonradioactive and radiative rates; k_B is the Boltzmann constant; Δ_E is the difference between the two excited energy levels [28].

S_r is also a very important parameter for temperature sensing, it refers to the relative change in Δ at a temperature change of 1 K, which can be used to quantitatively compare the performance of different optical thermometers. S_r can be expressed using the following formula [29]:

$$S_r = 100\% \times \frac{1}{\Delta_{int}} \frac{d\Delta_{int}}{dT} \quad 2$$

From Fig. 4c, we can see that data points of Δ_{int} at different temperatures fit well by the calibration curve ($R^2 = 0.996$), and it is linearly related to temperature ($\Delta_{int} = 0.03936 + 0.01075$ T). It can be seen from Fig. 4d that $NaYF_4$:Tm^{3+}, Er^{3+}@$NaYF_4$@SiO_2 have the highest S_r at 298K, $S_{rmax} = 0.36\%\ K^{-1}$. Therefore, physiological nanothermometers based on $NaYF_4$:Tm^{3+}, Er^{3+}@$NaYF_4$@SiO_2 with both excitation and emission in the NIR-II region may provide an efficient platform for in situ deep tissue temperature detection.

Temperature-dependent NIR emission spectra and contour map of $NaYF_4$:Yb^{3+}, Ho^{3+}@$NaYF_4$:Nd^{3+}@SiO_2 aqueous suspension under 808 nm excitation was presented in Fig. 5 The integrated emission intensity of $^2F_{5/2} \rightarrow {}^2F_{7/2}$ transition (Yb^{3+}) at 980 nm decreases with temperature increase, while the integrated emission intensity of $^5I_6 \rightarrow {}^5I_8$ transition (Ho^{3+}) at 1160 nm is almost unchanged with the change of temperature.

Temperature sensing performance of $NaYF_4$:Yb^{3+}, Ho^{3+}@$NaYF_4$:Nd^{3+}@SiO_2 were assessed by Δ_{int} and S_r mentioned above. Δ_{int} can be calculated using the following formula:

$$\Delta_{int} = \frac{I_{Yb}}{I_{Ho}} = \frac{\Delta_0}{1 + \alpha \exp(-\frac{\Delta E}{k_B T})} \quad 3$$

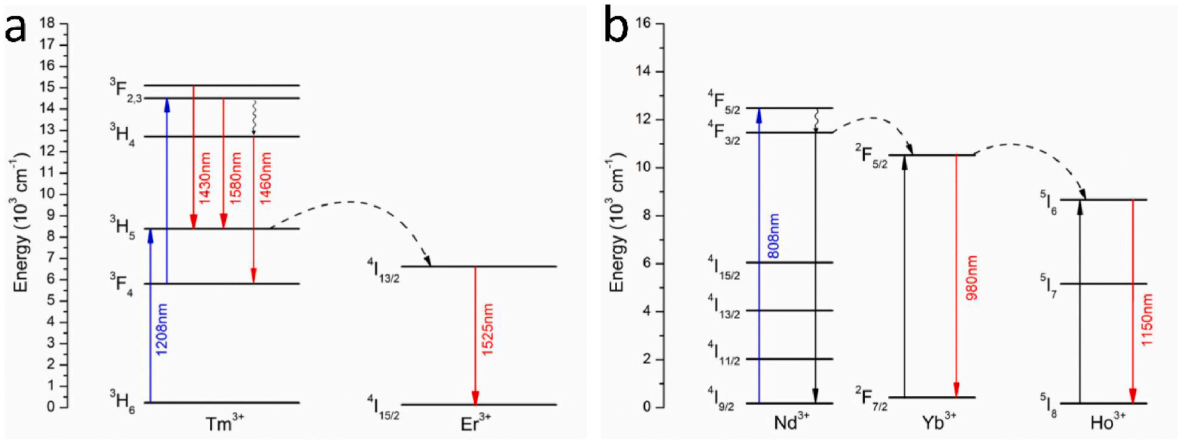

Fig. 6. Schematic energy level diagram for (a) Tm^{3+} and Er^{3+} and the emission mechanism under 808 nm excitation; (b) Yb^{3+}, Ho^{3+} and Nd^{3+} and the emission mechanism under 1208 nm excitation.

Table 1
Comparison of temperature sensitive optical parameter for the chosen reported materials.

Nanothermometers	Excitation (nm)	λ (nm)	S_r (% K^{-1})	Reference	T (K)
$NaGdF_4$: Nd^{3+} & PbS/CdS/ZnS@PLGA	808	1060/1250	2.5	[32]	283–338
YVO_4: Nd^{3+}	808	1063/1071	0.15	[33]	123–873
$NaYF_4$: Yb^{3+}, Ho^{3+}, Er^{3+}	980	1150/1550	1.87	[34]	298–329
LaF_3: Nd^{3+}, Yb^{3+}	790	1000/1350	0.41	[35]	283–333
LaF_3: Nd^{3+}@Yb^{3+}	808	1350/1000	0.74	[36]	288–333
$NaYF_4$:2%Tm^{3+},5% Er^{3+}@$NaYF_4$@SiO_2	1208	1460/1525	0.37	This work	298–353
$NaYF_4$:30%Yb^{3+},5% Ho^{3+}@$NaYF_4$:30% Nd^{3+}@SiO_2	808	980/1150	0.76	This work	298–353

Where I_{Yb} and I_{Ho} are the integrated emission intensity of Yb^{3+} at 980 nm and Ho^{3+} at 1160 nm, respectively. The Δ_{int} data at different temperatures match the calibration curve (Fig. 5c) very well ($R^2 = 0.999$), Δ_{int} and temperature are linearly dependent ($\Delta_{int} = 128.79267–0.48317\ T + 4.86275 \times 10^{-4}\ T^2$), It can be seen from Fig. 5d that the $NaYF_4$:Yb^{3+}, Ho^{3+}@$NaYF_4$:Nd^{3+}@SiO_2 has the highest S_r at 343K, $S_{rmax} = 0.76\%\ K^{-1}$. Therefore, $NaYF_4$:Yb^{3+}, Ho^{3+}@$NaYF_4$:Nd^{3+}@SiO_2 can be used as a nanothermometer in the physiological temperature range.

The regularly change in Δ_{int} of Tm^{3+}/Er^{3+} or Yb^{3+}/Ho^{3+} couple with the increased temperature may be closely related to the energy transfer (ET) between Ln^{3+}. The schematic energy level diagram for Tm^{3+} and Er^{3+} is shown in Fig. 6a. Tm^{3+} absorbs a 1208 nm photon and transits from the ground state $^3H_6$ to the excited state $^3H_5$ through ground state absorption (GSA), then energy is transferred to the excited state $^4I_{13/2}$ of Er^{3+} by ET process, and back to the ground state ($^4I_{15/2}$) by radiation transition, resulting in a 1525 nm emission. Besides, the ground state $^3F_4$ of Tm^{3+} captures a 1208 nm photon to fill the excited state $^3F_3$ via excited state absorption (ESA), and then reaches the excited state $^3H_4$ through multi-phonon-assisted relaxation (MPR), finally radiatively transits to the ground state $^3F_4$ and the emission 1460 nm emanated. The MPR process is gradually enhanced with temperature increase [30], so I_{Tm} increases with the increase of temperature. ET from energy level $^3H_5$ to $^4I_{13/2}$ occurs in the Tm^{3+}-Er^{3+} system instead of MPR, and ET process is not affected by temperature, so I_{Er} is insensitive to temperature changes.

Fig. 6b presents the schematic energy level diagram for Nd^{3+}, Yb^{3+} and Ho^{3+}. Nd^{3+} absorbs an 808 nm photon and is activated from the ground state $^4I_{9/2}$ to the excited state $^4F_{5/2}$ by GSA, then relax to the excited state $^4F_{3/2}$. The energy from $^4F_{3/2}$ of Nd^{3+} transits to $^2F_{5/2}$ of Yb^{3+} through multi phonon-assisted energy transfer, then back to the ground state $^2F_{7/2}$ by radiation transition, resulting in a 980 nm emission. The partial excitation energy of $^2F_{5/2}$ of Yb^{3+}transfers to the excited state $^5I_6$ of Ho^{3+} through multi phonon-assisted energy transfer, and then back to the ground state $^5I_8$ by radiation transition by emitting 1150 nm emission. In general, I_{Yb} at 980 nm should also enhance as the multi phonon-assisted energy transfer process from Nd^{3+} to Yb^{3+} is gradually enhanced with temperature increase, however, I_{Yb} shows a decreasing trend with the raising temperature, due to efficient multi phonon-assisted energy transfer from $^2F_{5/2}$ of Yb^{3+} to $^5I_6$ of Ho^{3+}. In addition, I_{Ho} at 1150 nm basically remains unchanged due to the stretching O–H mode from water shifts to higher energies with the increased temperature, giving enhanced water assisted non-radiative relaxation from $^5I_6$ to $^5I_8$ of Ho^{3+} [31].

Table 1 lists excitation and emission wavelengths, S_r, temperature range of some typical nanothermometers based on different Ln^{3+} doped materials. The synthesized $NaYF_4$:Tm^{3+}, Er^{3+}@$NaYF_4$@SiO_2 and $NaYF_4$:Yb^{3+}, Ho^{3+}@$NaYF_4$:Nd^{3+}@SiO_2 reveal favorable temperature sensing capability, moreover, the two nanotherometers are both operated in physiological temperature range, the excitation and emission wavelengths of $NaYF_4$:Tm^{3+}, Er^{3+}@$NaYF_4$@SiO_2 are in the NIR-II region simultaneously, making them potentially for temperature sensing in biological systems.

3.3. Biosafety evaluation and in vitro penetration test

In order to prove the optical thermometry application of $NaYF_4$:Tm^{3+}, Er^{3+}@$NaYF_4$@SiO_2 and $NaYF_4$:Yb^{3+}, Ho^{3+}@$NaYF_4$:Nd^{3+}@SiO_2 in the deep tissue, we first evaluated their biocompatibility by the following experiments.

L929 mouse fibroblasts were used to verify the cytotoxicity of SiO_2 coated Ln^{3+} doped NPs. Fig. S8 shows the survival rates of L929 mouse fibroblasts cells are all above 80% at different concentrations, the results indicate that $NaYF_4$:Yb^{3+}, Ho^{3+}@$NaYF_4$:Nd^{3+} @SiO_2 and $NaYF_4$:Tm^{3+}, Er^{3+}@$NaYF_4$@SiO_2 NPs have desirable biocompatibility and low cytotoxicity.

The hemocompatibility of $NaYF_4$:Yb^{3+}, Ho^{3+}@$NaYF_4$:Nd^{3+} @SiO_2 and $NaYF_4$:Tm^{3+}, Er^{3+}@$NaYF_4$@SiO_2 NPs was assessed using a hemolysis assay, and the hemolysis rate can reflect the interaction strength of NPs and erythrocytes. If the hemolysis rate of NPs is less than 5%, meaning that they have good hemocompatibility and meet the requirements for hemolysis of medical materials. Fig. S8 shows the

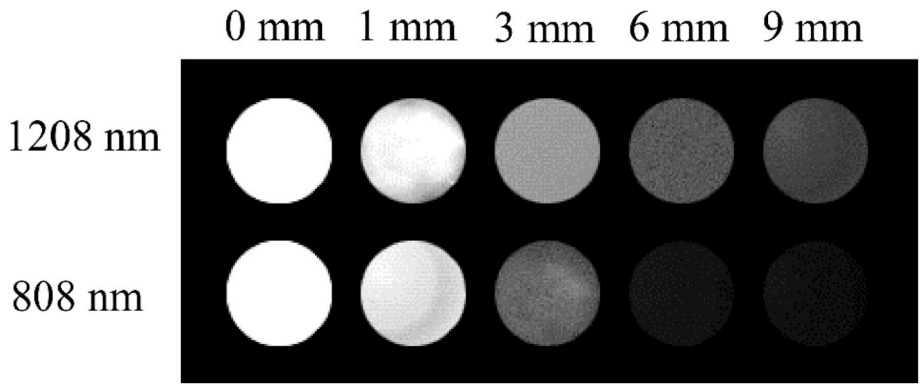

Fig. 7. Comparison of the NIR-II emission signals of $NaYF_4:Tm^{3+}$, $Er^{3+}@NaYF_4@SiO_2$ under 1208 nm laser excitation and $NaYF_4:Yb^{3+}$, $Ho^{3+}@NaYF_4:Nd^{3+}@SiO_2$ under 808 nm laser excitation in various thicknesses of pork muscle tissues.

hemolysis rates of the red blood cells incubated with two NPs are all below 5% at different concentrations, indicating the two NPs did not produce obvious hemolytic effects, and are capable of satisfactory hemocompatibility.

To assess in vivo toxicity of SiO_2 coated NPs, blood biochemical and histological analyses were performed. The photographs of H&E staining of major organs collected from BALB/c mice. Fig. S7 shows the main organs of mice have no obvious abnormality. In addition, routine blood analysis was performed including red blood cells (RBC), white blood cells (WBC), hemoglobin (HGB), hematocrit (HCT), platelets (PLT), mean corpuscular hemoglobin (MCH), mean corpuscular hemoglobin concentration (MCHC) and mean corpuscular volume (MCV) (Fig. S6), the results show that most of the parameters are within the normal level. All biosafety evaluations prove excellent biocompatibility of NPs and the potential for in vivo thermometry.

Subsequently, we investigated the penetration depth of $NaYF_4:Tm^{3+}$, $Er^{3+}@NaYF_4@SiO_2$ and $NaYF_4:Yb^{3+}$, $Ho^{3+}@NaYF_4:Nd^{3+}@SiO_2$ in vitro. Fig. 7 shows NIR-II emission signals follow a gradient decay trend with increased tissue depth, and which of $NaYF_4:Tm^{3+}$, $Er^{3+}@NaYF_4@SiO_2$ can be detected through 9 mm pork muscle tissue; while the emission signals of $NaYF_4:Yb^{3+}$, $Ho^{3+}@NaYF_4:Nd^{3+}@SiO_2$ disappears when the thickness of pork muscle tissue reaches to 6 mm. The NIR-II fluorescence imaging has the advantages of strong penetrability and low tissue attenuation compared to the NIR-I fluorescence imaging. Therefore, $NaYF_4:Tm^{3+}$, $Er^{3+}@NaYF_4@SiO_2$ with NIR-II excitation and emission is more suitable for deep tissue temperature detection in vivo.

4. Conclusion

In conclusion, we have synthesized two biocompatible Ln^{3+} doped NPs ($NaYF_4:Tm^{3+}$, $Er^{3+}@NaYF_4@SiO_2$ and $NaYF_4:Yb^{3+}$, $Ho^{3+}@NaYF_4:Nd^{3+}@SiO_2$), which exhibit the temperature-dependent NIR-II downshifting luminescence over the physiological temperature range under 1208 nm and 808 nm laser excitation, respectively. Regarding to $NaYF_4:Tm^{3+}$, $Er^{3+}@NaYF_4@SiO_2$ aqueous suspension, the NIR-II emission ratio between I_{Tm} at 1460 nm ($^3H_4 \rightarrow {}^3F_4$) and I_{Er} at 1525 nm ($^4I_{13/2} \rightarrow {}^4I_{13/2}$) gradually enhances with temperature increase, and the highest S_r is 0.36% K^{-1} at 298 K; while for $NaYF_4:Yb^{3+}$, $Ho^{3+}@NaYF_4:Nd^{3+}@SiO_2$ aqueous suspension, the emission ratio between I_{Yb} at 980 nm ($^2F_{5/2} \rightarrow {}^2F_{7/2}$) and I_{Ho} at 1150 nm ($^5I_6 \rightarrow {}^5I_8$) declines with the increase of temperature, and the highest Sr is 0.76% K^{-1} at 343 K. Good biocompatibility of the developed NPs is proved by hemolysis, cytotoxicity, mouse blood biochemistry, histology analysis. In vitro tissue penetration experiment demonstrates that the NIR-II emission has better tissue penetration over NIR-I emission. Both $NaYF_4:Tm^{3+}$, $Er^{3+}@NaYF_4@SiO_2$ and $NaYF_4:Yb^{3+}$, $Ho^{3+}@NaYF_4:Nd^{3+}@SiO_2$ NPs are suitable for deep tissue temperature sensing, while $NaYF_4:Tm^{3+}$, $Er^{3+}@NaYF_4@SiO_2$ with NIR-II excitation and emission displays better performance in deep tissue temperature detection. This work exploits a strategy for the development of NIR-II luminescent nanothermometers, via selecting suitable Ln^{3+} combinations and doping concentration to regulate ET process.

Declaration of competing interest

The authors declare that they have no known competing financial interests or personal relationships that could have appeared to influence the work reported in this paper.

Acknowledgments

This research was supported by National Natural Science Foundation of China (NSFC) (Grant No. 52002336) China Postdoctoral Science Foundation (No.2022M711514, No.2022T150298), Fundamental Research Funds for the Central Universities (SWU019041), the Science and Technology project of Chongqing Education Committee (No. KJCX2020005), and the open project of State Key Laboratory of Marine Resource Utilization in South China Sea (No. MRUKF20210330), Chongqing Engineering Research Center for Rapid Diagnosis of Dread Disease and Chongqing Engineering Research Center for Micro-Nano Biomedical Materials and Devices, Southwest University, China. We thank Analytical and Testing Center of Southwest University for their assistance with FT-IR spectra analysis. We acknowledge critical and quantity of testing work supported by Beijing Zhong Ke Bai Ce Technology Service Co. We thank the temperature-dependent luminescence help of Xuan Zhang and Ran Liu from Edinburgh instruments.

Appendix A. Supplementary data

Supplementary data to this article can be found online at https://doi.org/10.1016/j.ceramint.2022.08.110.

References

[1] L.J. Mohammed, K.M. Omer, Carbon dots as new generation materials for nanothermometer: review, Nanoscale Res. Lett. 15 (2020) 182, https://doi.org/10.1186/s11671-020-03413-x.

[2] B. Yang, X. Li, Y. Hou, A. Meier, X. Cheng, J.-H. Choi, F. Wang, H. Wang, A. Wagner, D. Yan, A. Li, T. Olofsson, H. Li, Non-invasive (non-contact) measurements of human thermal physiology signals and thermal comfort/discomfort poses-A review, Energy Build. 224 (2020), 110261, https://doi.org/10.1016/j.enbuild.2020.110261.

[3] F. Vetrone, R. Naccache, A. Zamarrón, A. Juarranz de la Fuente, F. Sanz-Rodríguez, L. Martinez Maestro, E. Martín Rodriguez, D. Jaque, J. García Solé, J. A. Capobianco, Temperature sensing using fluorescent nanothermometers, ACS Nano 4 (2010) 3254–3258, https://doi.org/10.1021/nn100244a.

[4] D. Chen, S. Liu, Z. Wan, Z. Ji, EuF_3/Ga_2O_3 Dual-phase nanostructural glass ceramics with Eu^{2+}/Cr^{3+} dual-activator luminescence for self-calibrated optical

thermometry, J. Phys. Chem. C 120 (2016) 21858–21865, https://doi.org/10.1021/acs.jpcc.6b08271.
[5] D. Chen, M. Xu, S. Liu, X. Li, Eu^{2+}/Eu^{3+} dual-emitting glass ceramic for self-calibrated optical thermometry, Sens. Actuators, B 246 (2017) 756–760, https://doi.org/10.1016/j.snb.2017.02.159.
[6] W. Xu, Y. Hu, L. Zheng, Z. Zhang, W. Cao, H. Liu, X. Wu, Enhanced NIR-NIR luminescence from $CaWO_4$: Nd^{3+}/Yb^{3+} phosphors by Li^+ codoping for thermometry and optical heating, J. Lumin. 208 (2019) 415–423, https://doi.org/10.1016/j.jlumin.2019.01.005.
[7] Y. Zhang, S. Xu, X. Li, J. Zhang, J. Sun, H. Xia, R. Hua, B. Chen, Fabrication, photothermal conversion and temperature sensing of novel nanoplatform-hybrid nanocomposite of $NaYF_4$:Er^{3+},Yb^{3+}@$NaYF_4$ and Au nanorods for photothermal therapy, Mater. Res. Bull. 114 (2019) 148–155, https://doi.org/10.1016/j.materresbull.2019.03.003.
[8] Y. Zhao, X. Wang, Y. Zhang, Y. Li, X. Yao, Optical temperature sensing of up-conversion luminescent materials: fundamentals and progress, J. Alloys Compd. 817 (2020), 152691, https://doi.org/10.1016/j.jallcom.2019.152691.
[9] S.-N. Zhao, L.-J. Li, X.-Z. Song, M. Zhu, Z.-M. Hao, X. Meng, L.-L. Wu, J. Feng, S.-Y. Song, C. Wang, H.-J. Zhang, Lanthanide ion codoped emitters for tailoring emission trajectory and temperature sensing, Adv. Funct. Mater. 25 (2015) 1463–1469, https://doi.org/10.1002/adfm.201402061.
[10] D. Chen, W. Xu, Y. Zhou, Y. Chen, Lanthanide doped $BaTiO_3SrTiO_3$ solid-solution phosphors: structure, optical spectroscopy and upconverted temperature sensing behavior, J. Alloys Compd. 676 (2016) 215–223, https://doi.org/10.1016/j.jallcom.2016.03.201.
[11] D. Chen, W. Xu, S. Yuan, X. Li, J. Zhong, Ln^{3+}-Sensitized Mn^{4+} near-infrared upconverting luminescence and dual-modal temperature sensing, J. Mater. Chem. C 5 (2017) 9619–9628, https://doi.org/10.1039/C7TC02182H.
[12] G.-L. Law, W.-M. Kwok, W.-T. Wong, K.-L. Wong, P.A. Tanner, Terbium luminescence sensitized through three-photon excitation in a self-assembled unlinked antenna, J. Phys. Chem. B 111 (2007) 10858–10861, https://doi.org 10.1021/jp.0755185.
[13] G.-L. Law, K.-L. Wong, K.-K. Lau, S.-t. Lap, P.A. Tanner, F. Kuo, W.-T. Wong, Nonlinear optical activity in dipolar organic–lanthanide complexes, J. Mater. Chem. 20 (2010) 4074–4079, https://doi.org 10.1039/b926376d.
[14] D.K. Chatterjee, A.J. Rufaihah, Y. Zhang, Upconversion fluorescence imaging of cells and small animals using lanthanide doped nanocrystals, Biomaterials 29 (2008) 937–943, https://doi.org/10.1016/j.biomaterials.2007.10.051.
[15] H. Li, X. Wang, T.Y. Ohulchanskyy, G. Chen, Lanthanide-doped near-infrared nanoparticles for biophotonics, Adv. Mater. 33 (2021), 2000678, https://doi.org/10.1002/adma.202000678.
[16] B. Li, L. Lu, M. Zhao, Z. Lei, F. Zhang, An efficient 1064 nm NIR-II excitation fluorescent molecular dye for deep-tissue high-resolution dynamic bioimaging, Angew. Chem., Int. Ed. Engl. 57 (2018) 7483–7487, https://doi.org/10.1002/ange.201801226.
[17] G. Hong, A.L. Antaris, H. Dai, Near-infrared fluorophores for biomedical imaging, Nat. Biomed. Eng. 1 (2017), 0010, https://doi.org/10.1038/s41551-016-0010.
[18] S. Ding, L. Lu, Y. Fan, F. Zhang, Recent progress in NIR-II emitting lanthanide-based nanoparticles and their biological applications, J. Rare Earths 38 (2020) 451–463, https://doi.org/10.1016/j.jre.2020.01.021.
[19] M. Runowski, N. Stopikowska, D. Szeremeta, S. Goderski, M. Skwierczynska, S. Lis, Upconverting lanthanide fluoride core@shell nanorods for luminescent thermometry in the first and second biological windows: beta-NaYF4:Yb^{3+} - Er^{3+}@SiO_2 temperature sensor, ACS Appl. Mater. Interfaces 11 (2019) 13389–13396, https://doi.org/10.1021/acsami.9b00445.
[20] X. Xu, Z. Wang, P. Lei, Y. Yu, S. Yao, S. Song, X. Liu, Y. Su, L. Dong, J. Feng, H. Zhang, Alpha-NaYb(Mn)F4:Er^{3+}/Tm^{3+}@$NaYF_4$ UCNPs as "band-shape" luminescent nanothermometers over a wide temperature range, ACS Appl. Mater. Interfaces 7 (2015) 20813–20819, https://doi.org/10.1021/acsami.5b05876.
[21] T. Grzyb, P. Kaminski, D. Przybylska, A. Tyminski, F. Sanz-Rodriguez, P. Haro Gonzalez, Manipulation of up-conversion emission in NaYF4 core@shell nanoparticles doped by Er^{3+}, Tm^{3+}, or Yb^{3+} ions by excitation wavelength-three ions-plenty of possibilities, Nanoscale 13 (2021) 7322–7333, https://doi.org/10.1039/D0NR07136F.
[22] X.-F. Yu, L.-D. Chen, M. Li, M.-Y. Xie, L. Zhou, Y. Li, Q.-Q. Wang, Highly efficient fluorescence of NdF_3/SiO_2 core/shell nanoparticles and the applications for in vivo NIR detection, Adv. Mater. 20 (2008) 4118–4123, https://doi.org/10.1002/adma.200801224.
[23] A. Szczeszak, A. Ekner-Grzyb, M. Runowski, K. Szutkowski, L. Mrówczyńska, Z. Kaźmierczak, T. Grzyb, K. Dąbrowska, M. Giersig, S. Lis, Spectroscopic, structural and in vitro cytotoxicity evaluation of luminescent, lanthanide doped core@shell nanomaterials $GdVO_4$:Eu^{3+}5%@SiO_2@NH_2, J. Colloid Interface Sci. 481 (2016) 245–255, https://doi.org/10.1016/j.jcis.2016.07.025.
[24] M. Runowski, K. Dąbrowska, T. Grzyb, P. Miernikiewicz, S. Lis, Core/shell-type nanorods of Tb^{3+}-doped $LaPO_4$, modified with amine groups, revealing reduced cytotoxicity, J. Nanoparticle Res. 15 (2013) 2068, https://doi.org/10.1007/s11051-013-2068-5.
[25] J.-C. Boyer, L.A. Cuccia, J.A. Capobianco, Synthesis of colloidal upconverting $NaYF_4$: Er^{3+}/Yb^{3+} and Tm^{3+}/Yb^{3+} monodisperse nanocrystals, Nano Lett. 7 (2007) 847–852, https://doi.org/10.1021/nl070235+.
[26] C. Cao, H.K. Yang, J.W. Chung, B.K. Moon, B.C. Choi, J.H. Jeong, K.H. Kim, Hydrothermal synthesis and white luminescence of Dy^{3+}-doped $NaYF_4$ microcrystals, J. Am. Ceram. Soc. 94 (2011) 3405–3411, https://doi.org/10.1111/j.1551-2916.2011.04518.x.
[27] H. Zhang, Y. Xiao, F. Qi, P. Liu, Y. Wang, F. Li, C. Wang, G. Fang, X. Zhao, Near-infrared light-sensitive hole-transport-layer free perovskite solar cells and photodetectors with hexagonal NaYF4:Yb^{3+},Tm^{3+}@SiO_2 upconversion nanoprism-modified TiO_2 scaffold, ACS Sustainable Chem. Eng. 7 (2019) 8236–8244, https://doi.org/10.1021/acssuschemeng.8b06606.
[28] A.M. Kaczmarek, M.K. Kaczmarek, R. Van Deun, Er^{3+}-to-Yb^{3+} and Pr^{3+}-to-Yb^{3+} energy transfer for highly efficient near-infrared cryogenic optical temperature sensing, Nanoscale 11 (2019) 833–837, https://doi.org/10.1039/C8NR08348G.
[29] L. Wortmann, S. Suyari, T. Ube, M. Kamimura, K. Soga, Tuning the thermal sensitivity of β-NaYF4: Yb^{3+}, Ho^{3+}, Er^{3+} nanothermometers for optimal temperature sensing in OTN-NIR (NIR II/III) biological window, J. Lumin. 198 (2018) 236–242, https://doi.org/10.1016/j.jlumin.2018.01.049.
[30] M. Szalkowski, M. Dudek, Z. Korczak, C. Lee, Ł. Marciniak, E.M. Chan, P.J. Schuck, A. Bednarkiewicz, Predicting the impact of temperature dependent multi-phonon relaxation processes on the photon avalanche behavior in Tm^{3+}:$NaYF_4$ nanoparticles, Opt. Mater. X 12 (2021), 100102, https://doi.org/10.1016/j.omx.2021.100102.
[31] A. Skripka, A. Benayas, R. Marin, P. Canton, E. Hemmer, F. Vetrone, Double rare-earth nanothermometer in aqueous media: opening the third optical transparency window to temperature sensing, Nanoscale 9 (2017) 3079–3085, https://doi.org/10.1039/C6NR08472A.
[32] E.N. Cerón, D.H. Ortgies, B. del Rosal, F. Ren, A. Benayas, F. Vetrone, D. Ma, F. Sanz-Rodríguez, J.G. Solé, D. Jaque, E.M. Rodríguez, Hybrid nanostructures for high-sensitivity luminescence nanothermometry in the second biological window, Adv. Mater. 27 (2015) 4781–4787, https://doi.org/10.1002/adma.201501014.
[33] I.E. Kolesnikov, A.A. Kalinichev, M.A. Kurochkin, E.V. Golyeva, E.Y. Kolesnikov, A. V. Kurochkin, E. Lähderanta, M.D. Mikhailov, YVO_4:Nd^{3+} nanophosphors as NIR-to-NIR thermal sensors in wide temperature range, Sci. Rep. 7 (2017), 18002, https://doi.org/10.1038/s41598-017-18295-w.
[34] S. Sekiyama, M. Umezawa, S. Kuraoka, T. Ube, M. Kamimura, K. Soga, Temperature sensing of deep abdominal region in mice by using over-1000 nm near-infrared luminescence of rare-earth-doped $NaYF_4$ nanothermometer, Sci. Rep. 8 (2018), 16979, https://doi.org/10.1038/s41598-018-35354-y.
[35] E.C. Ximendes, W.Q. Santos, U. Rocha, U.K. Kagola, F. Sanz-Rodríguez, N. Fernández, A.d.S. Gouveia-Neto, D. Bravo, A.M. Domingo, B. del Rosal, C.D. S. Brites, L.D. Carlos, D. Jaque, C. Jacinto, Unveiling in vivo subcutaneous thermal dynamics by infrared luminescent nanothermometers, Nano Lett. 16 (2016) 1695–1703, https://doi.org/10.1021/acs.nanolett.5b04611.
[36] E.C. Ximendes, U. Rocha, K.U. Kumar, C. Jacinto, D. Jaque, LaF_3 core/shell nanoparticles for subcutaneous heating and thermal sensing in the second biological-window, Appl. Phys. Lett. 108 (2016), 253103, https://doi.org/10.1063/1.4954170.